Electronic Supplementary Information

Rational design of oxide/carbon composite to achieve superior rate-capability *via* enhanced lithium-ion transport across carbon to oxide

Jun Hui Jeong[a], Myeong-Seong Kim[a], Yeon Jun Choi[a], Geon-Woo Lee[a], Byung Hoon Park[a], Suk-Woo Lee[a], Kwang Chul Roh[b,*] and Kwang-Bum Kim[a,*]

[a] Department of Materials Science and Engineering, Yonsei University, 50 Yonsei-ro, Seodaemun-gu, Seoul 03722, Republic of Korea

[b] Energy and Environmental Division, Korea Institute of Ceramic Engineering and Technology, 101 Soho-ro, Jinju-si, Gyeongsangnam-do, 52851, Republic of Korea.

* Corresponding authors.

E-mail addresses: rkc@kicet.re.kr (K. C. Roh), kbkim@yonsei.ac.kr (K. B. Kim)

Table S1. Brunauer–Emmett–Teller (BET) specific surface areas and pore volumes of LTO/rGO, LTO/L-NPG, LTO/M-NPG, and LTO/H-NPG composites

	BET surface area ($m^2\ g^{-1}$)	Pore Volume ($cm^3\ g^{-1}$)
LTO/rGO	25.4	0.208
LTO/L-NPG	43.7	0.311
LTO/M-NPG	44.1	0.327
LTO/H-NPG	41.9	0.364

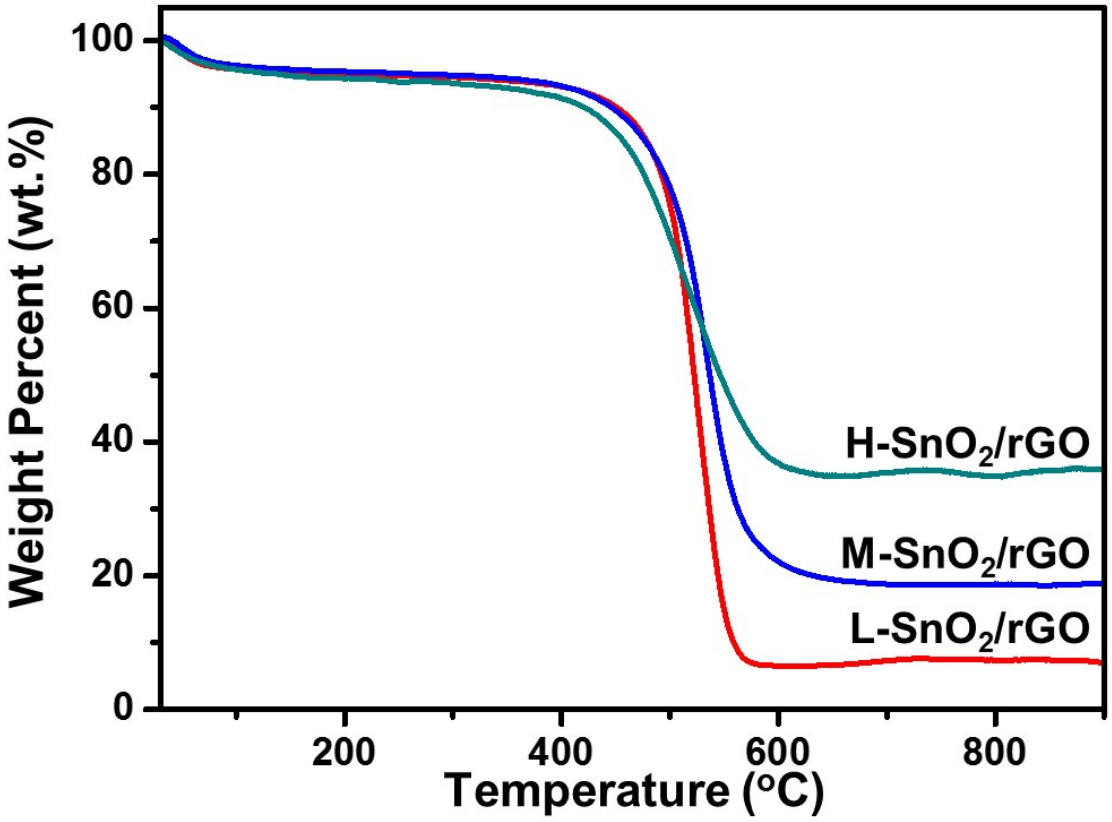

Fig. S1. TGA profiles of SnO_2/rGO composites with different loading amounts of SnO_2.

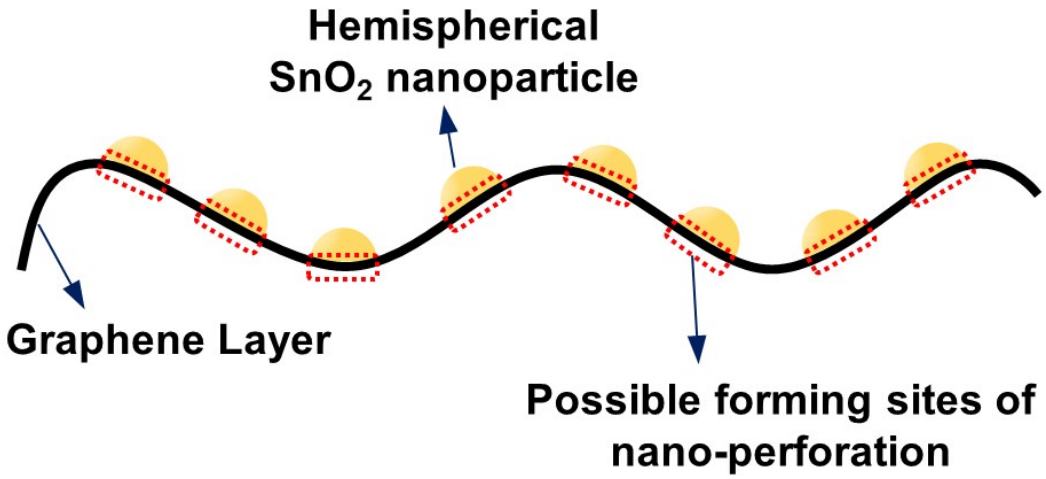

Fig. S2. Schematic diagram of SnO_2/rGO composite illustrating hemispherical SnO_2 nanoparticles deposited on the basal plane of graphene.

As illustrated in Fig. S2, we assumed the hemispherical SnO_2 nanoparticles deposited on the basal plane of graphene in calculating the number of nano-perforations in the NPG. Since nano-perforations were created only at the contact points with the hemispherical SnO_2 nanoparticles, number of nano-perforations in the NPG was determined by the number of hemispherical SnO_2 nanoparticles in the composite. The number of SnO_2 nanoparticles (N), which is equivalent to the number of nano-perforations, in the composites was calculated by dividing the weight of SnO_2 in SnO_2/rGO composites by the weight of a single hemispherical SnO_2 nanoparticle.

$$N = (Wx/100)/\{(4\pi r^3\rho/3)/2\} \qquad \text{(Eq. S1)}$$

where W is the weight of SnO_2/rGO composite (g) used for TGA, x is the weight percent of SnO_2 nanoparticles in SnO_2/rGO composite (wt%) from TGA, r is the radius of a SnO_2 nanoparticle (3 nm), ρ is the density of SnO_2 (6.95 g cm^{-3}).

As the weight percent of SnO_2 nanoparticles in SnO_2/rGO composite increases, the weight percent of rGO in SnO_2/rGO composite decreases. Therefore, the area of rGO available for SnO_2 nanoparticle deposition decreases. Finally, number density of nano-perforations, which is the number of nano-perforations per unit area, in the NPG was calculated as follows: (1) the area of rGO (S, m^2) available for SnO_2 nanoparticle deposition in SnO_2/rGO composite was calculated by multiplying the weight of rGO in the composite and the specific surface area of rGO; and (2) the number density of nano-perforations in the NPG (μm^{-2}) was calculated by dividing the number of nano-perforations in the NPG by the area of rGO in SnO_2/rGO composite:

$$S = W\{1-(x/100)\}A \quad \text{(Eq. S2)}$$

$$Number\ Density = N/S \quad \text{(Eq. S3)}$$

where A is the specific surface area of rGO (300 $m^2\ g^{-1}$) measured in BET analysis.

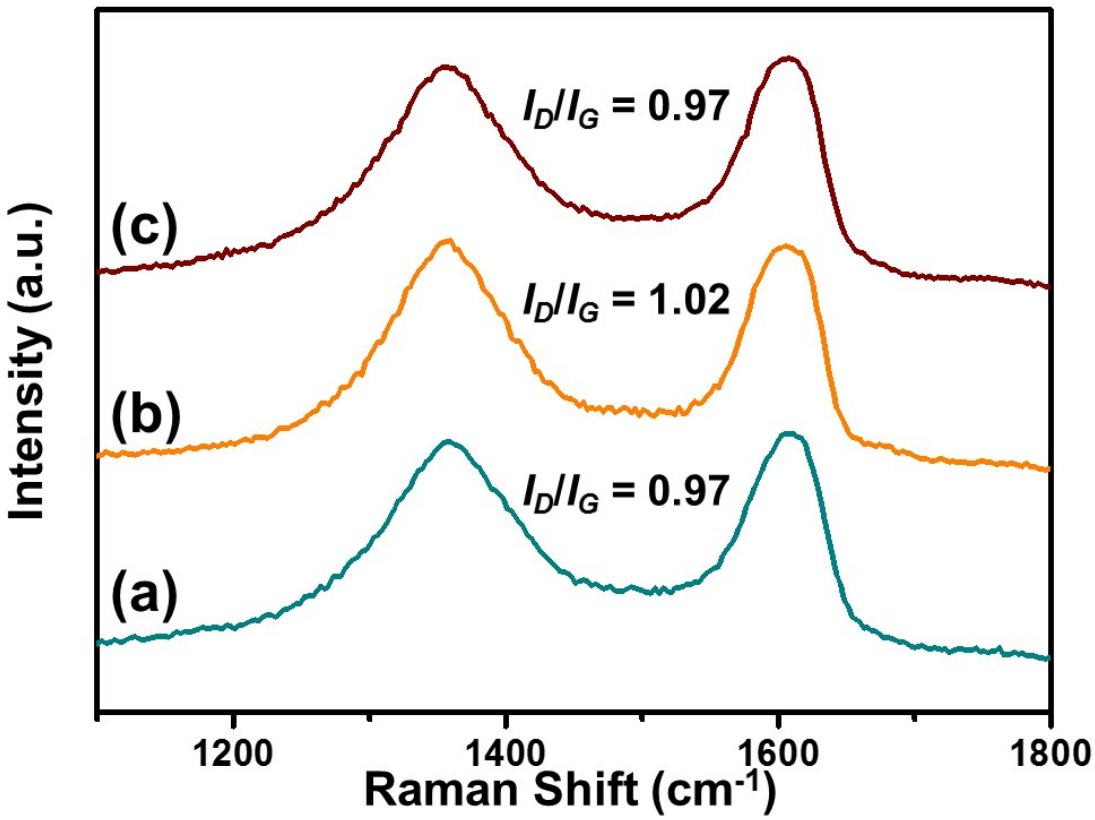

Fig. S3. Raman spectra of (a) NPG, (b) acid-treated NPG (a-NPG), and (c) heat-treated a-NPG.

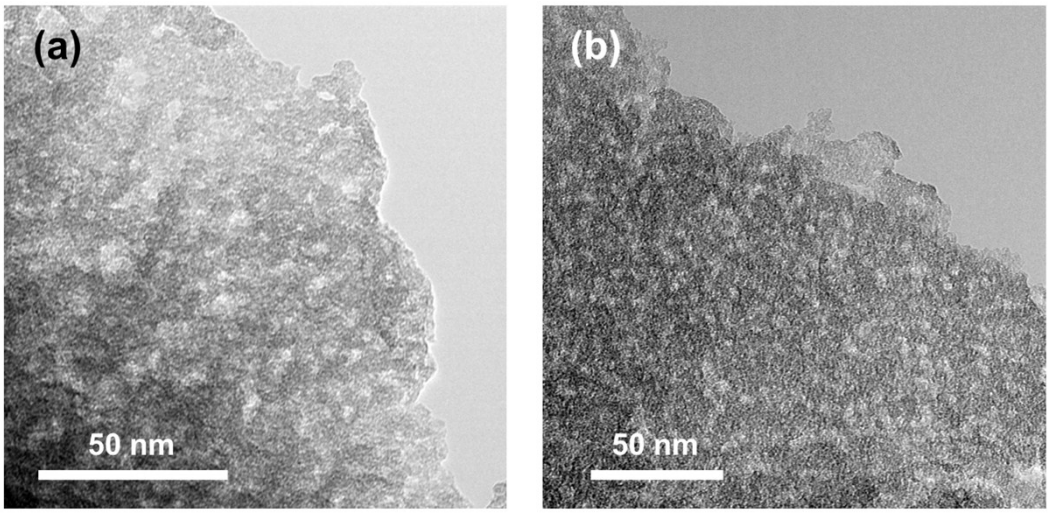

Fig. S4. TEM images of (a) a-NPG and (b) heat-treated a-NPG.

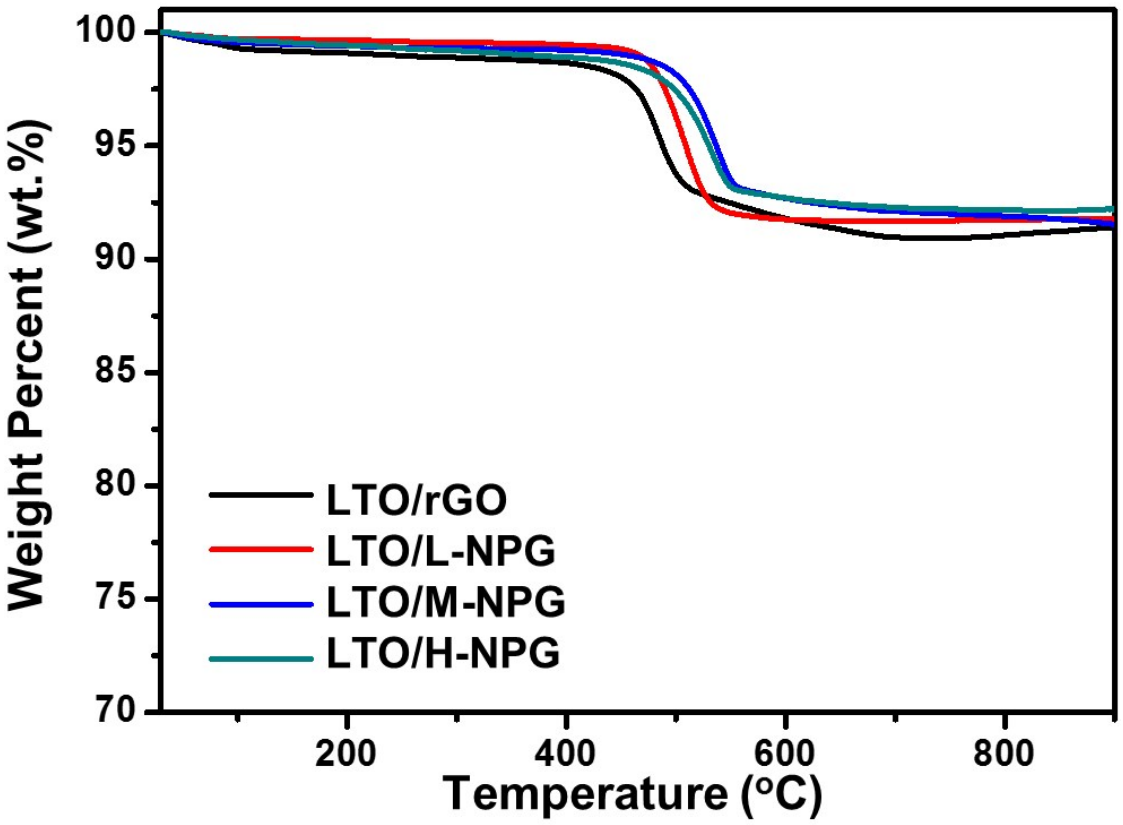

Fig. S5. TGA profiles of LTO/rGO, LTO/L-NPG, LTO/M-NPG, and LTO/H-NPG composites.

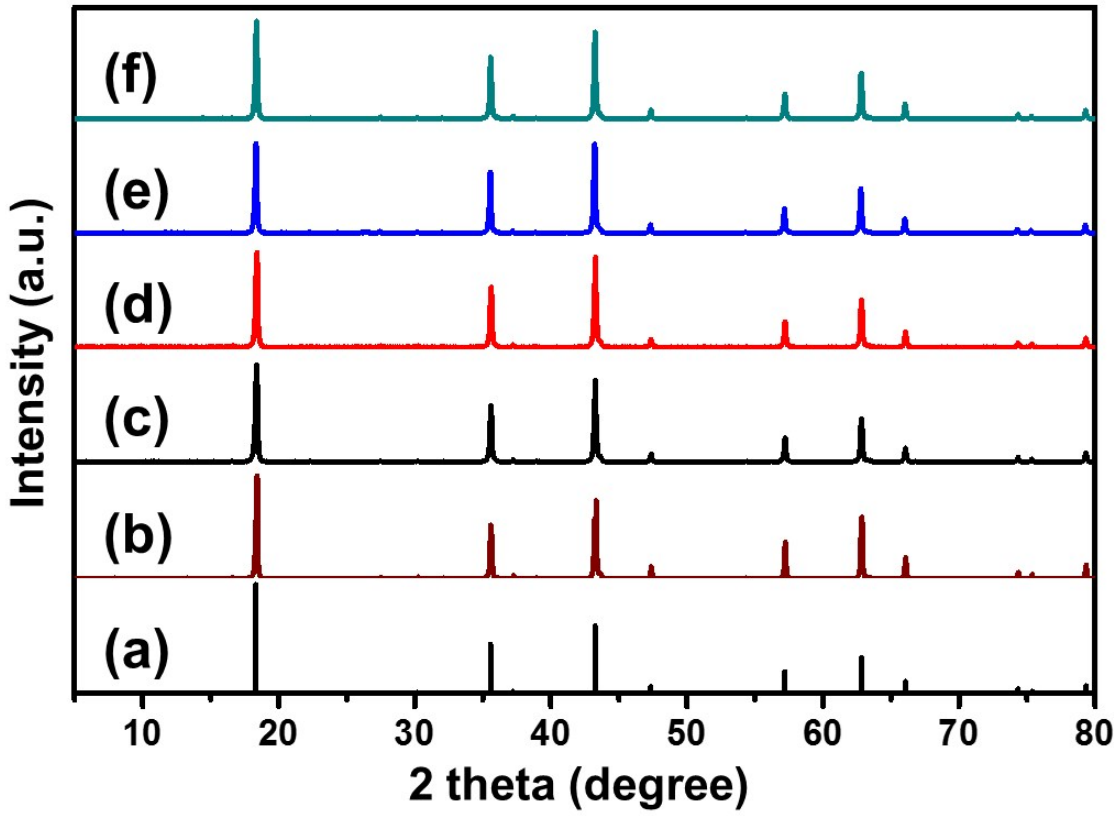

Fig. S6. XRD patterns of (a) JCPDS card No. 490207, (b) bare LTO, (c) LTO/rGO composite, (d) LTO/L-NPG composite, (e) LTO/M-NPG composite, and (f) LTO/H-NPG composite.

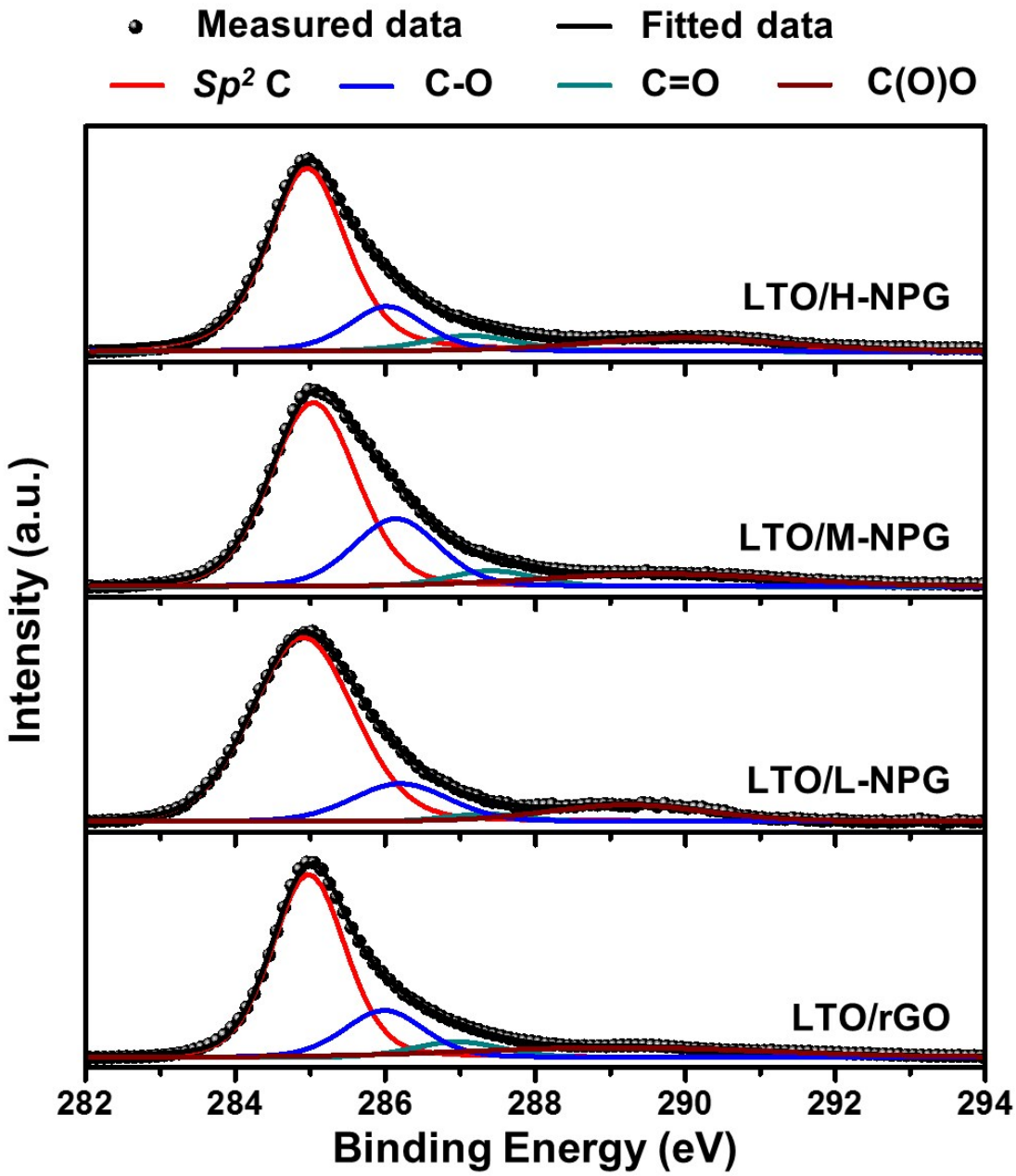

Fig. S7. XPS C1*s* spectra of LTO/rGO, LTO/L-NPG, LTO/M-NPG, and LTO/H-NPG composites.

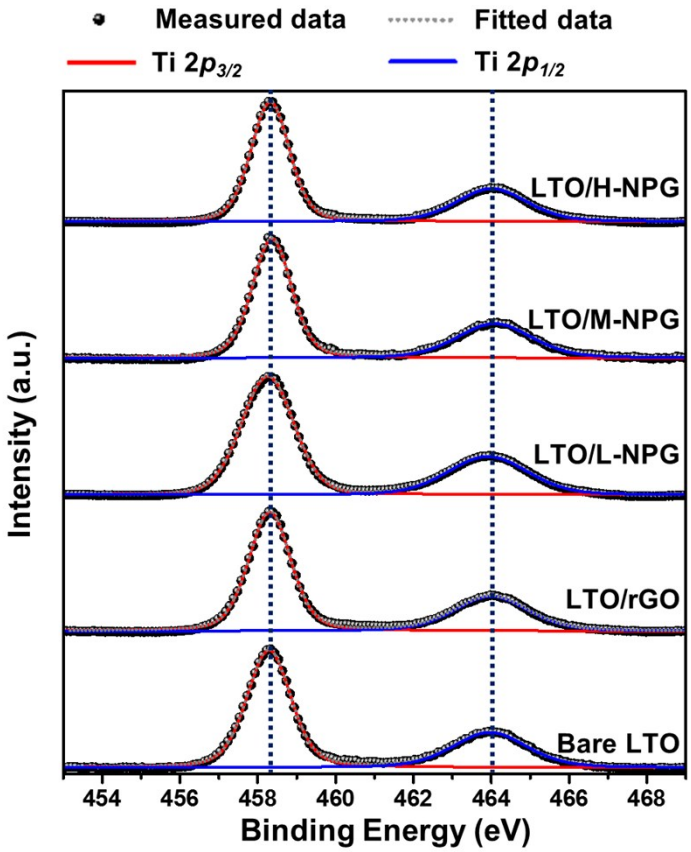

Fig. S8. XPS Ti 2*p* spectra of bare LTO and LTO/rGO, LTO/L-NPG, LTO/M-NPG, and LTO/H-NPG composites.

The Ti2*p* XPS spectra of bare LTO and LTO/rGO, LTO/L-NPG, LTO/M-NPG, and LTO/H-NPG composites were analyzed to investigate the oxidation state of Ti in the composites (Fig. S8†). All the LTO composites and bare LTO could be deconvoluted into two different peaks centered at 458.3 and 464.0 eV, corresponding to Ti2$p_{2/3}$ and Ti2$p_{1/2}$, respectively, which was the characteristic peaks of Ti^{4+}. In addition, the binding energy difference of 5.7 eV between the two peaks was observed for all the LTO composites and bare LTO, indicating that the oxidation state of Ti was Ti^{4+}.

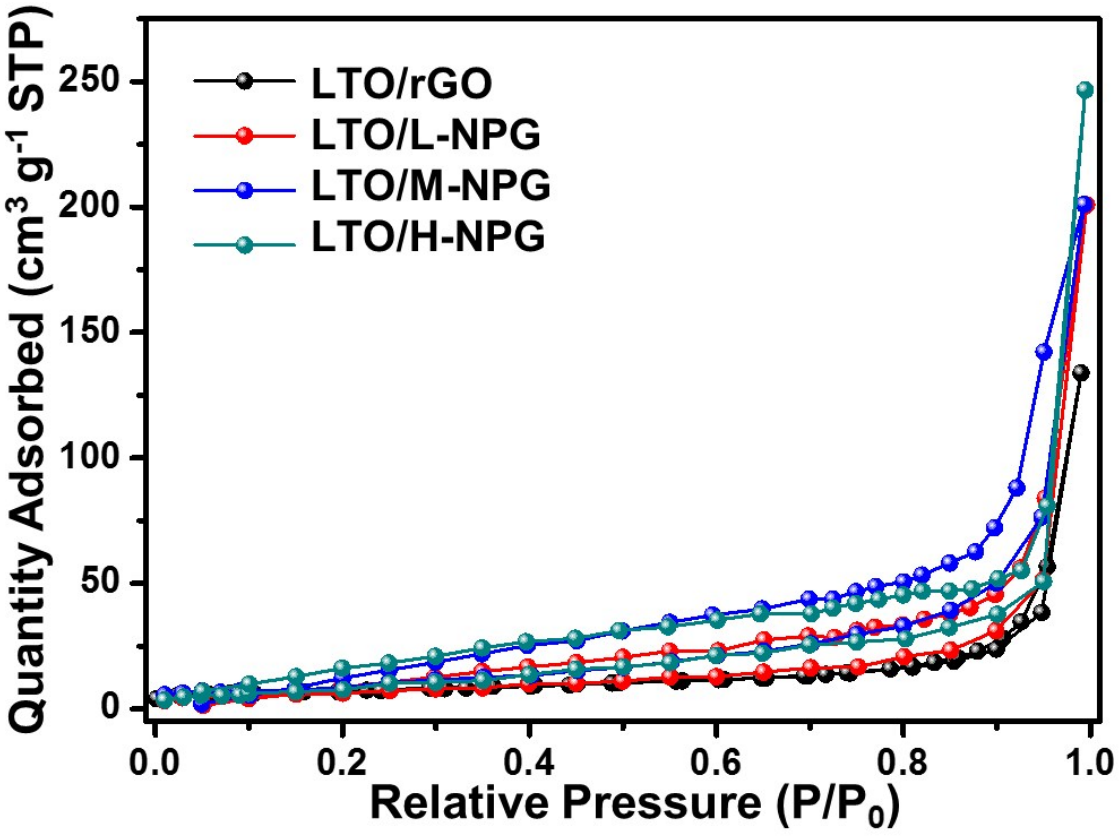

Fig. S9. N_2 gas adsorption/desorption isotherms of LTO/rGO, LTO/L-NPG, LTO/M-NPG, and LTO/H-NPG composites.

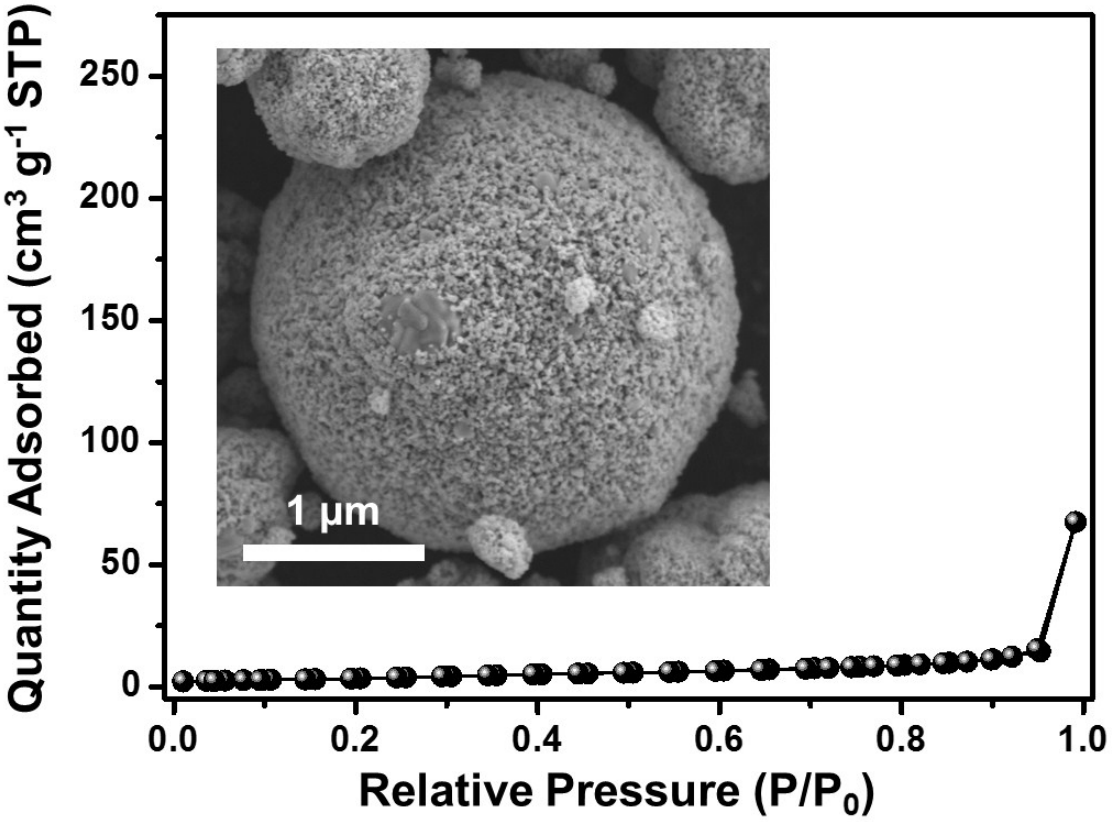

Fig. S10. SEM image (inset) and N_2 adsorption/desorption isotherms of pure LTO microspheres without NPG.

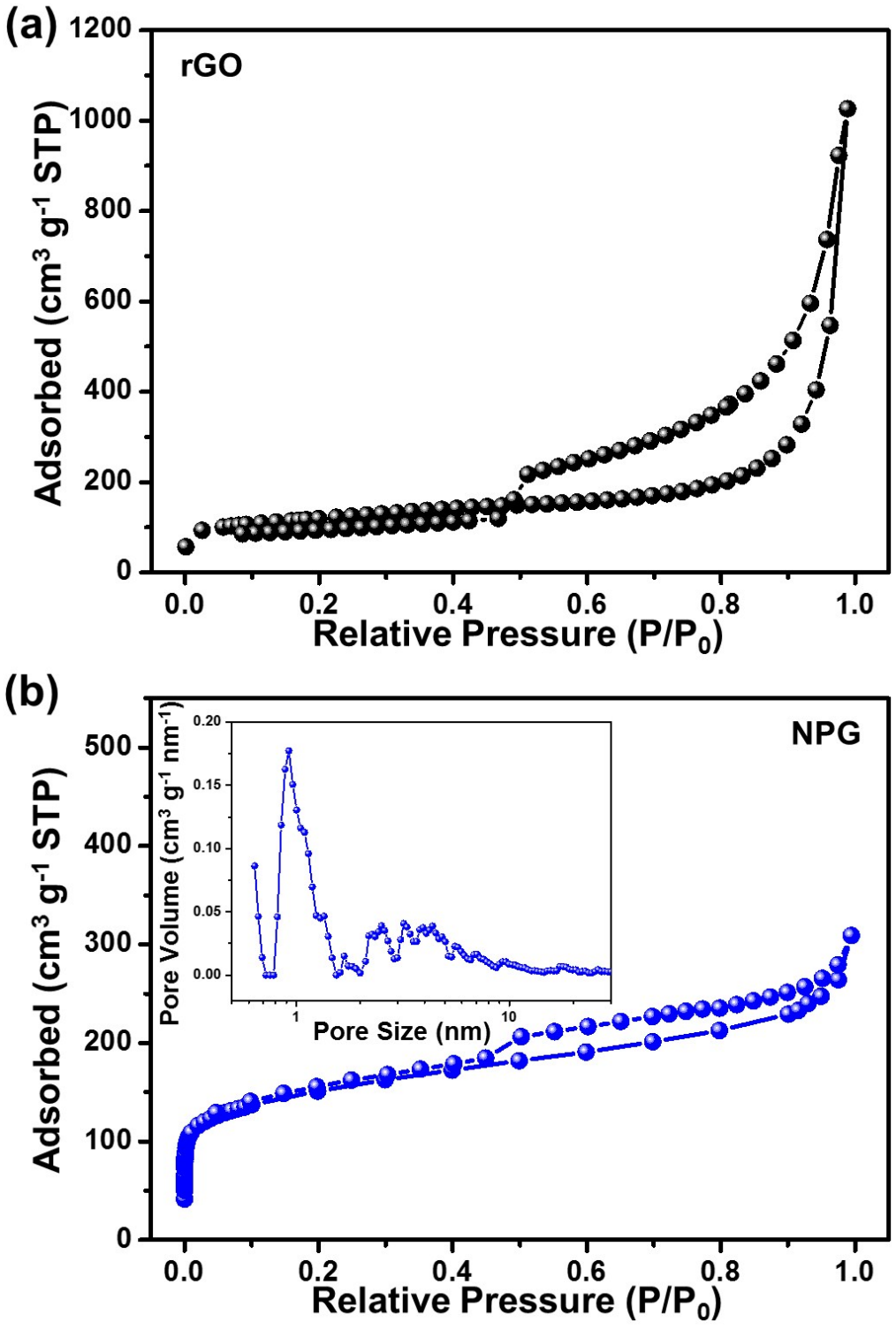

Fig. S11. N_2 adsorption/desorption isotherms of (a) rGO and (b) NPG.

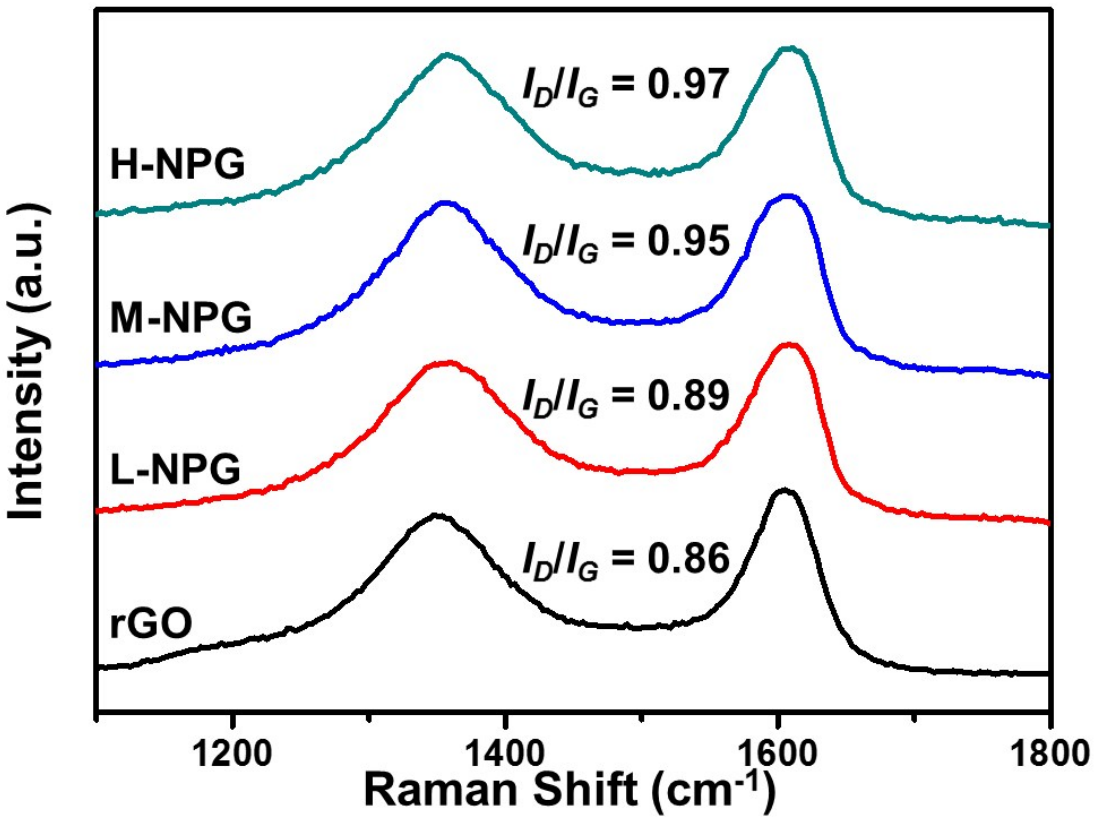

Fig. S12. Raman spectra of rGO, L-NPG, M-NPG, and H-NPG.

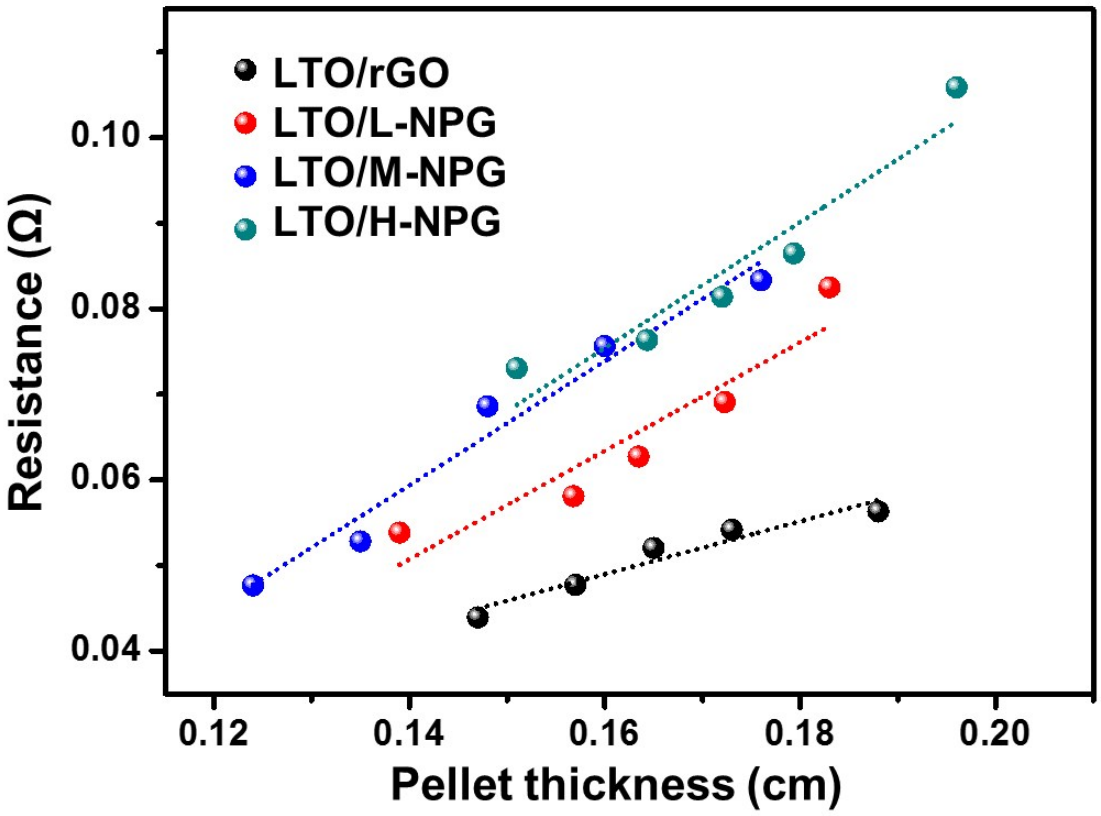

Fig. S13. Linear plot of the resistance as a function of the pellet thickness for calculating the electronic conductivity of LTO/rGO, LTO/L-NPG, LTO/M-NPG, and LTO/H-NPG composites.

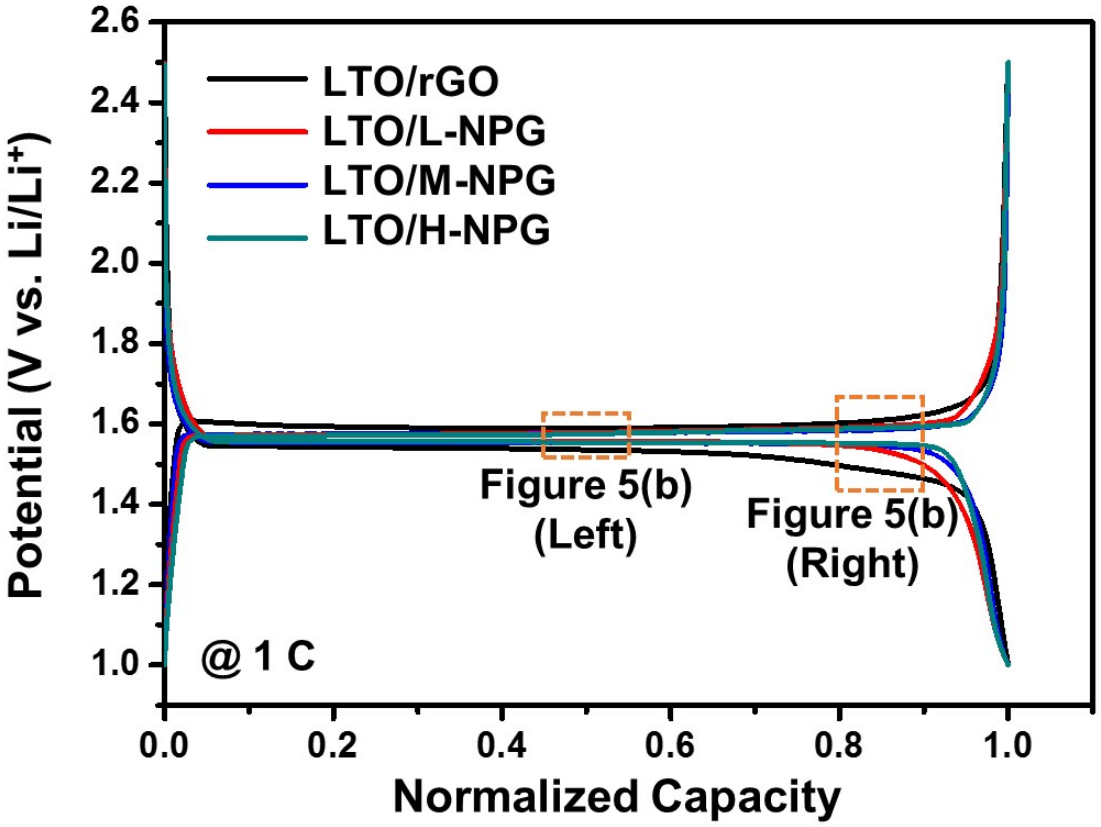

Fig. S14. GCD profiles of LTO/rGO, LTO/L-NPG, LTO/M-NPG, and LTO/H-NPG composites normalized with respect to the specific discharge capacities at 1 C.

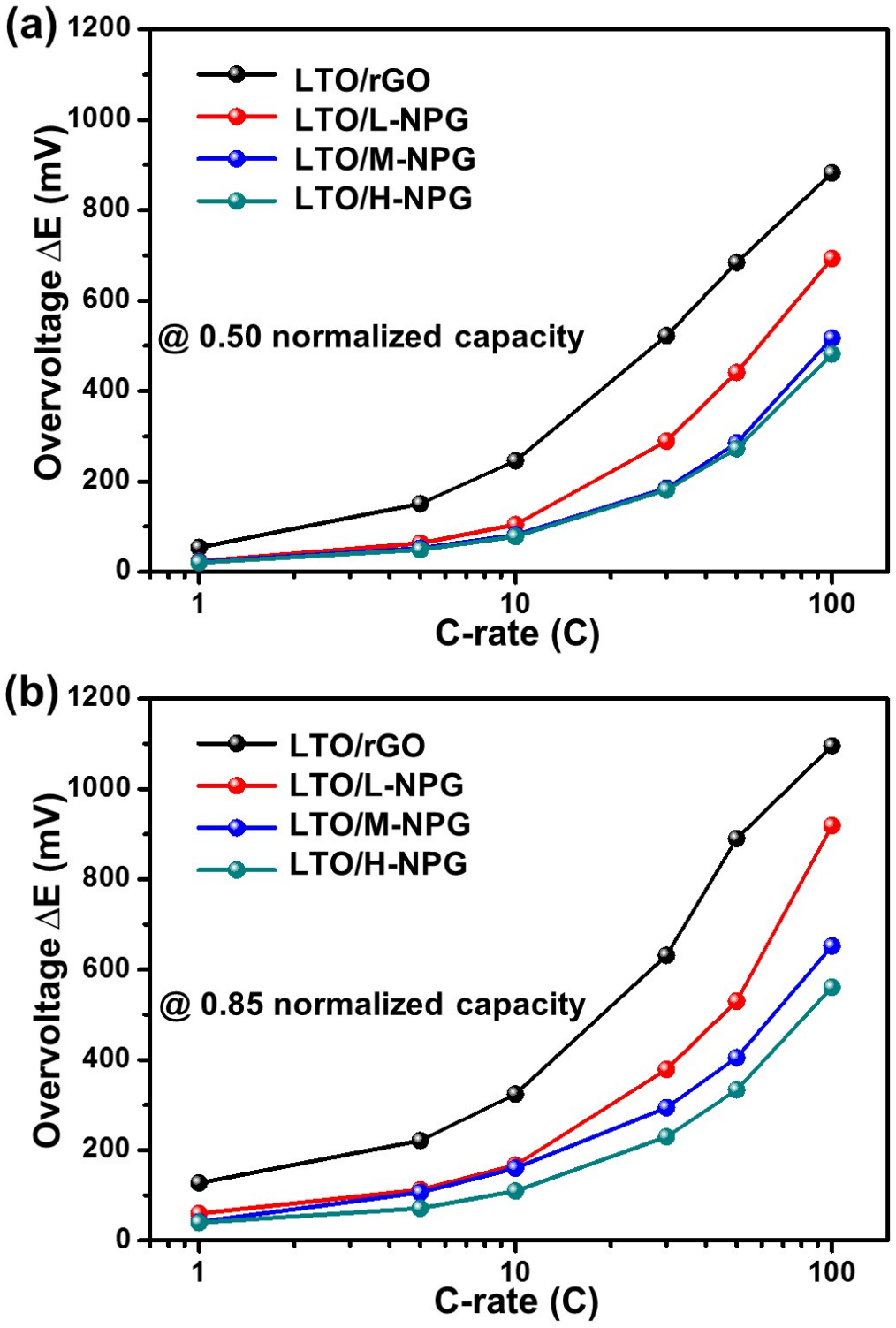

Fig. S15. Overvoltage plots of LTO/rGO, LTO/L-NPG, LTO/M-NPG, and LTO/H-NPG composites at normalized capacities of (a) 0.5 and (b) 0.85.

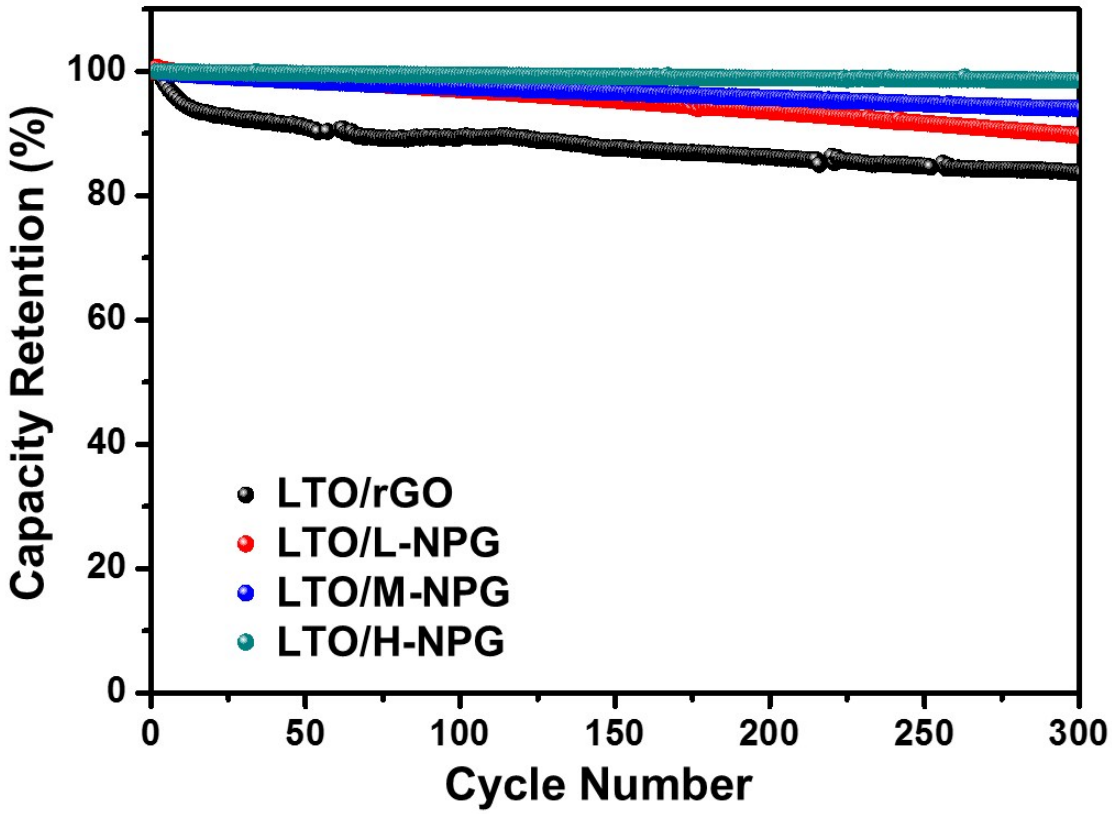

Fig. S16. Cycle performance of LTO/rGO, LTO/L-NPG, LTO/M-NPG, and LTO/H-NPG composites.

Fig. S16† compares the cyclabilities of LTO/rGO, LTO/L-NPG, LTO/M-NPG, and LTO/H-NPG composites over 300 cycles at 10 C. The LTO/NPG composites showed better cycling stabilities than LTO/rGO composite. After 300 cycles, LTO/rGO, LTO/L-NPG, LTO/M-NPG, and LTO/H-NPG composites could retain 83.7, 89.7, 95.4, and 98.6% of their initial discharge capacities, respectively.

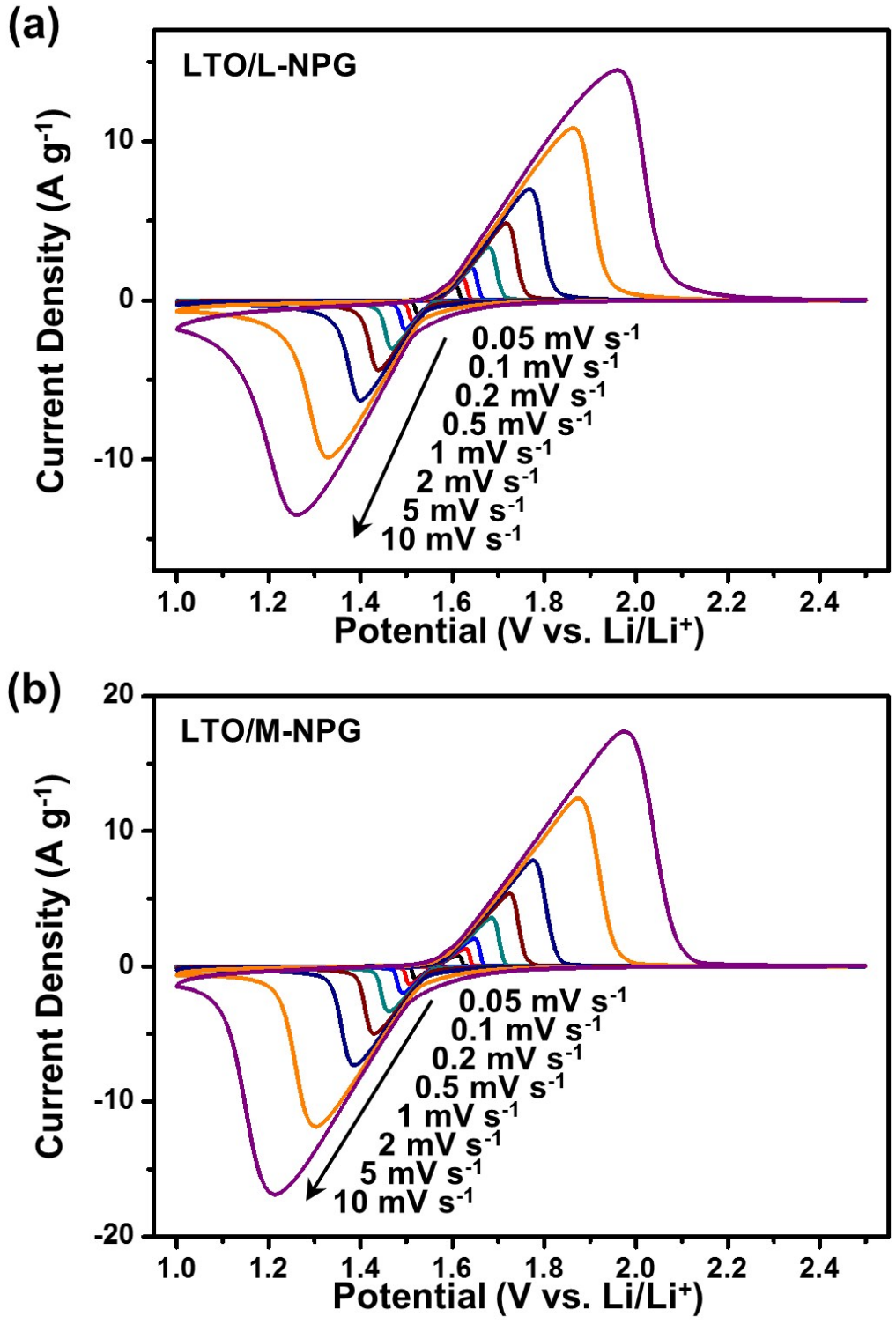

Fig. S17. CV profiles of (a) LTO/L-NPG and (b) LTO/M-NPG composites at increasing scan rates from 0.05 to 10 mV s^{-1}.

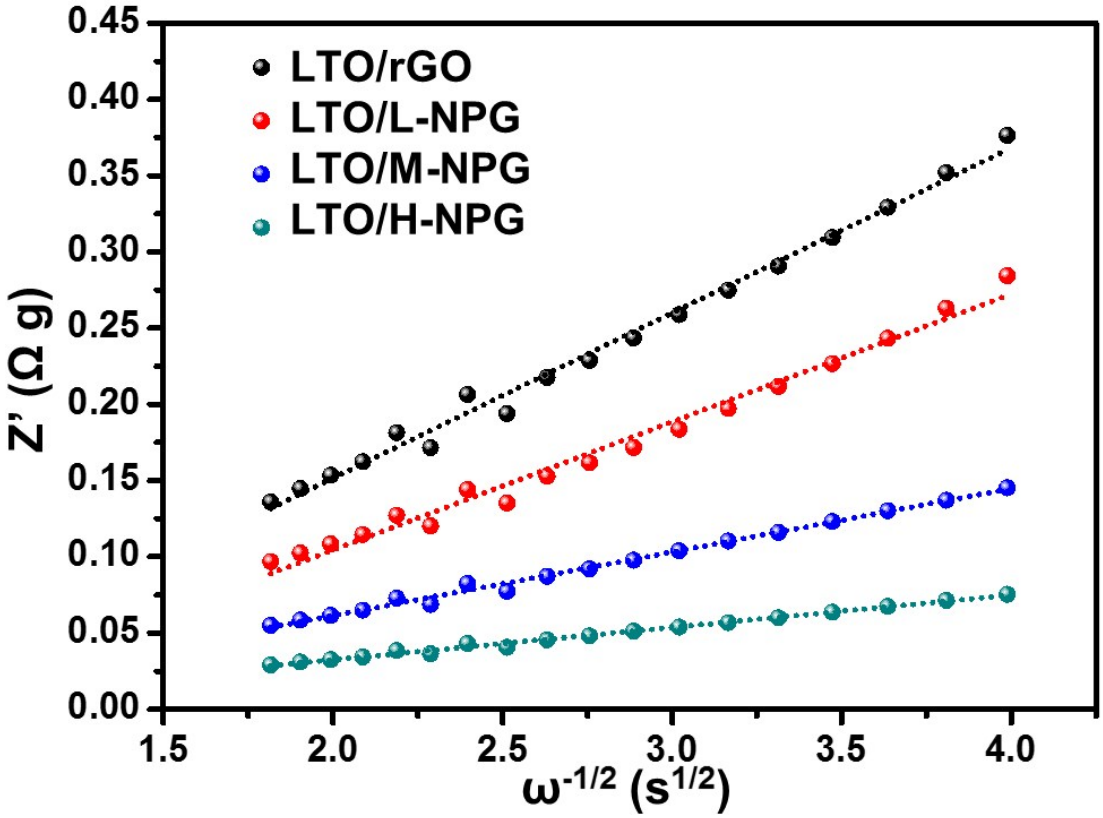

Fig. S18. Plot of real part of impedance vs. $\omega^{-1/2}$ (angular frequency$^{-1/2}$) for LTO/rGO, LTO/L-NPG, LTO/M-NPG and LTO/H-NPG composites.

To further analyze the EIS data of the LTO composites, the real part of the impedance in the low-frequency region (Z') was plotted against the reciprocal square root of the angular frequency ($\omega^{-1/2}$) at low frequencies in Fig. S18†. The linearity in Fig. S18† is associated with solid state diffusion of lithium ions in the bulk LTO. Equations S4 and S5 show the relationship between D_{app} and the Warburg factor (σ).

$$Z' = R_s + R_1 + R_{ct} + \sigma\omega^{-1/2} \qquad \text{(Eq. S4)}$$

$$D_{app} = (R^2T^2)/(2A^2n^4F^4C_{Li}^2\sigma^2) \qquad \text{(Eq. S5)}$$

where D_{app} is the apparent diffusion coefficient, R is the gas constant, T is the absolute temperature, A is the specific surface area of the electrochemically active sites ($m^2 \cdot g^{-1}$), n is the number of electrons per molecule during the reaction, F is the Faraday constant, C_{Li} is the concentration of the reactant, and σ is the Warburg factor calculated from the slope of the linear part of the EIS profiles between the real axis Z' and $\omega^{-1/2}$ using Equation S4.

In this EIS analysis, we again set D_{app} a constant (10^{-12} $cm^2 \cdot s^{-1}$) for LTO in the LTO composites according to the assumptions used for the CV data analysis using Randles–Sevcik equation Fig. 6(c). Finally, Equations S4 and S5 were used to calculate A for LTO/H-NPG, LTO/M-NPG, LTO/L-NPG, and LTO/rGO composites. A was calculated to be 4.327, 2.202, 1.092, and 0.847 $m^2 \cdot g^{-1}$ for LTO/H-NPG, LTO/M-NPG, LTO/L-NPG and LTO/rGO composites, respectively.

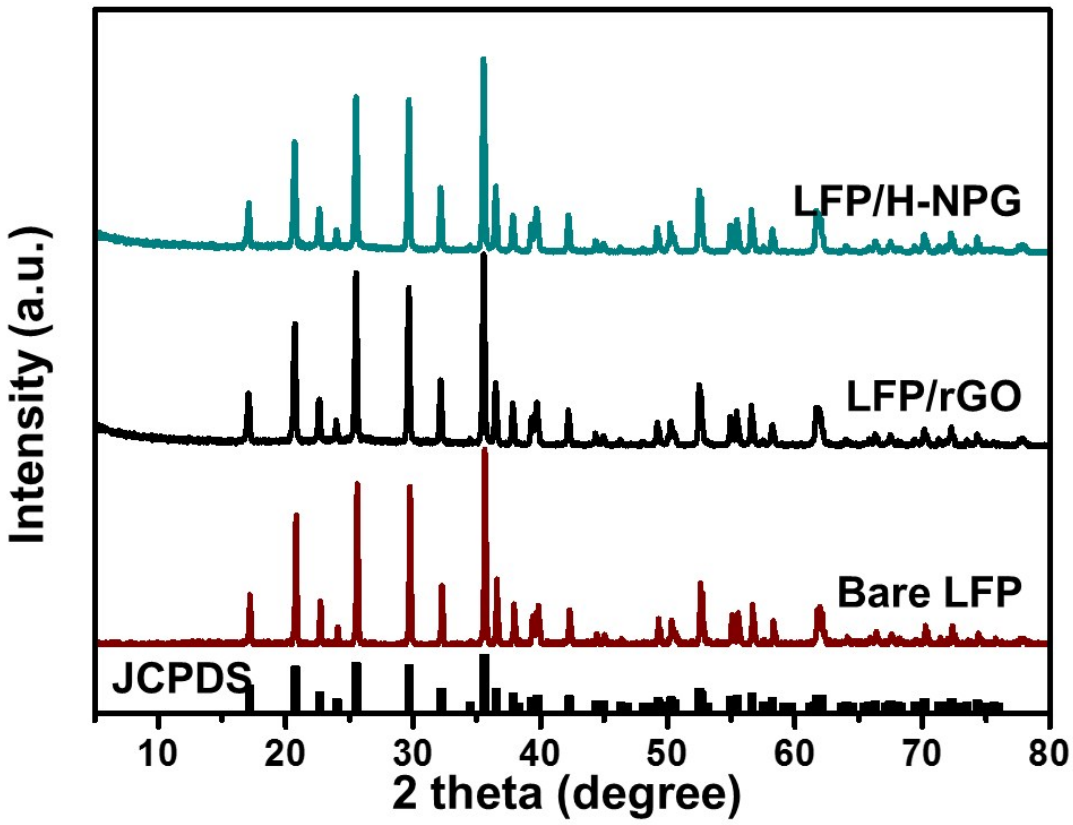

Fig. S19. XRD patterns of bare LFP, LFP/rGO composite, and LFP/H-NPG composite.

As shown in Fig. S19†, the XRD patterns of the LFP composites exhibited all the standard peaks observed for olivine LFP with the P_{nma} space group (JCPDS card No. 83-2092). No impurity peaks were observed in the XRD patterns of the LFP composites, indicating that the spray-drying process and heat treatment did not cause any structural changes of the olivine LFP.

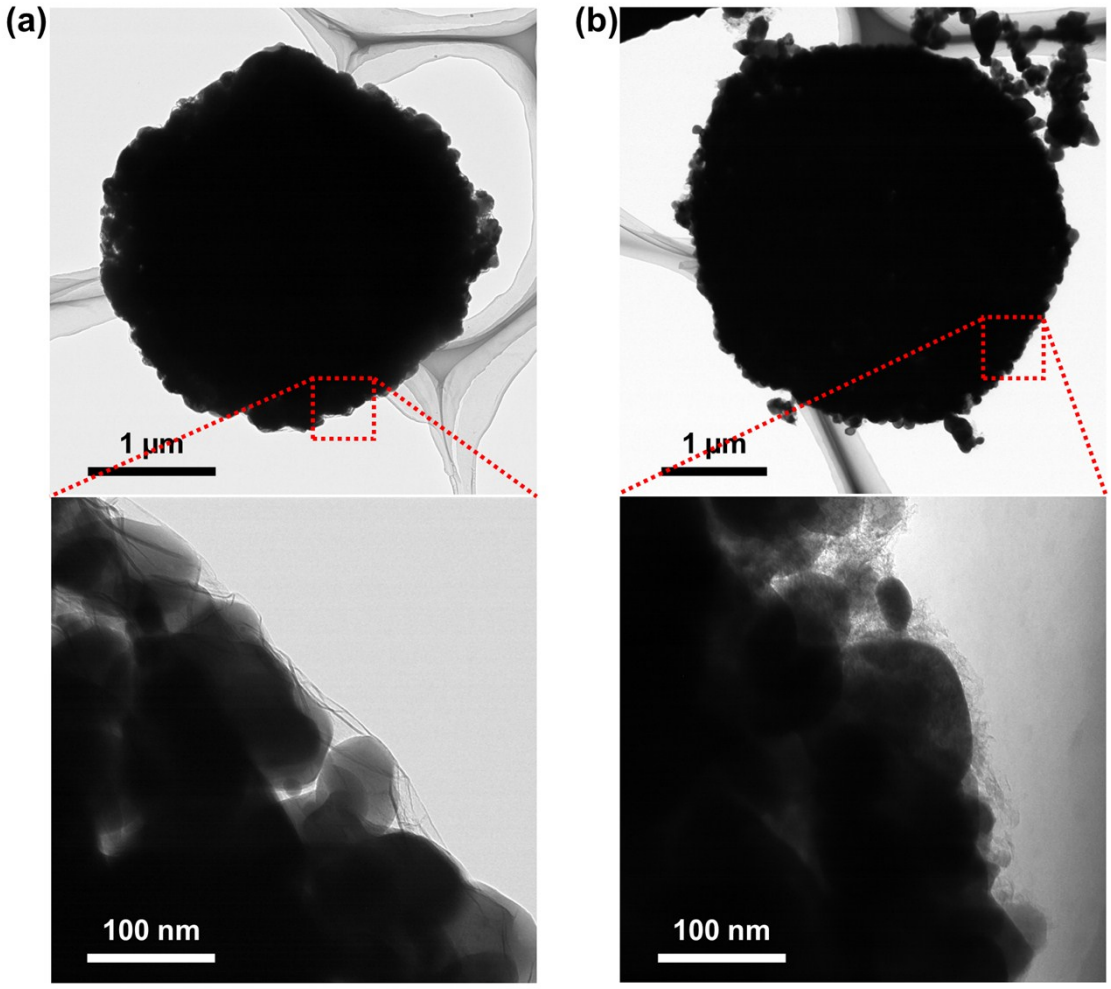

Fig. S20. TEM images of (a) LFP/rGO and (b) LFP/H-NPG composites.

Fig. S20† shows TEM images of LFP/rGO and LFP/H-NPG composites. A typical low-magnification TEM image reveals that the primary LFP nanoparticles were densely packed, consisting of secondary spherical micro-particles with diameters of ~3 μm. In addition, the appearance of the edge of an individual composite particle at higher magnification reveals that the LFP particles were wrapped by a thin layer of NPG (or rGO).

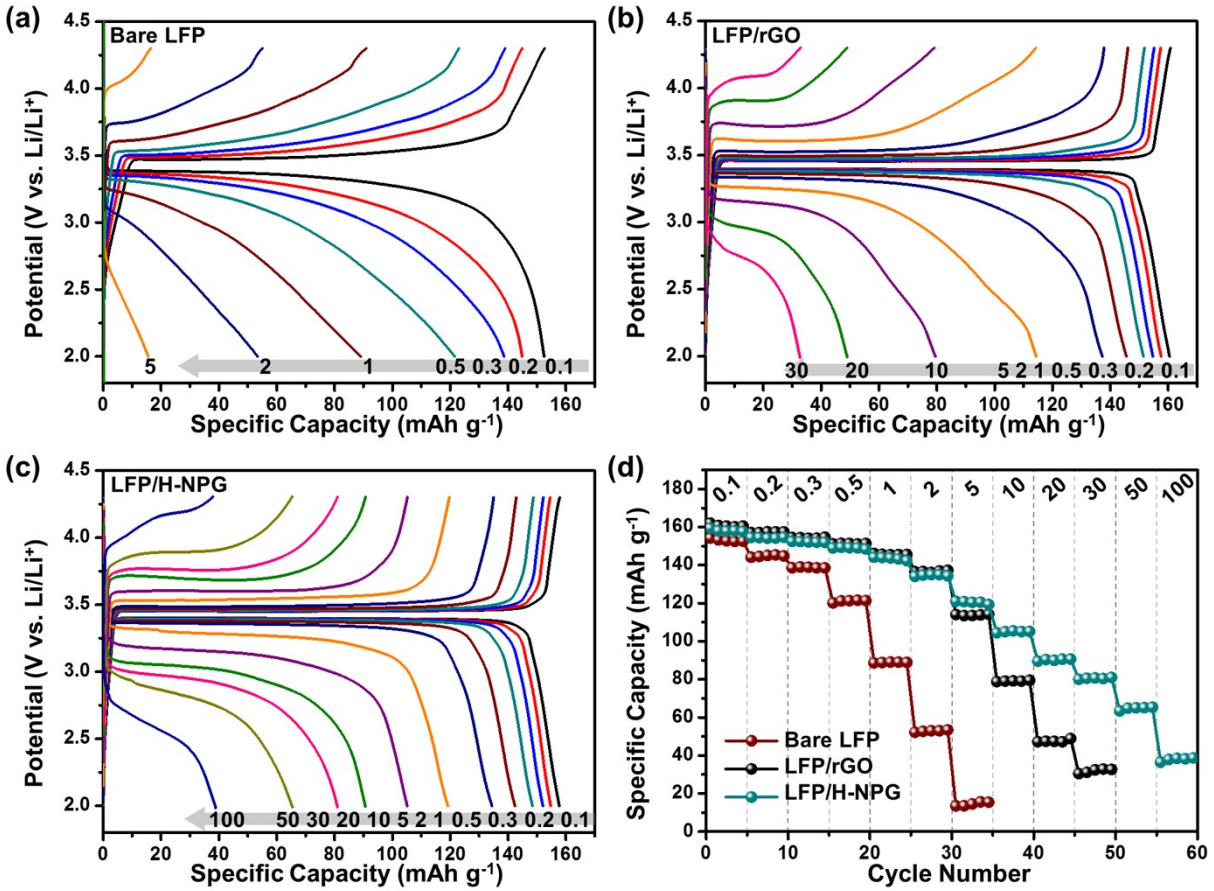

Fig. S21. Electrochemical properties of bare LFP, LFP/rGO composite and LFP/H-NPG composite in 1 M $LiPF_6$ 1:1 EC/DMC electrolyte in the 2.0–4.3 V potential window. The GCD profiles of (a) bare LFP, (b) LFP/rGO composite and (c) LFP/H-NPG composite at increasing C-rates from 0.1 to 100 C. (d) Plots of the rate capability of bare LFP, LFP/rGO composite, and LFP/H-NPG composite.